Zhang *et al. BioMed Eng OnLine* (2020) 19:51
https://doi.org/10.1186/s12938-020-00793-0

BioMedical Engineering OnLine

RESEARCH Open Access

Segmentation of small ground glass opacity pulmonary nodules based on Markov random field energy and Bayesian probability difference

Shaorong Zhang[1,3†], Xiangmeng Chen[4†], Zhibin Zhu[2*], Bao Feng[3,4], Yehang Chen[1] and Wansheng Long[4]

*Correspondence: optimization_zhu@163.com
†Shaorong Zhang and Xiangmeng Chen contributed equally to this work and should be considered co-first authors
[2] School of Mathematics and Computational Science, Guilin University of Electronic Technology, Guilin 541004, China
Full list of author information is available at the end of the article

Abstract

Background: Image segmentation is an important part of computer-aided diagnosis (CAD), the segmentation of small ground glass opacity (GGO) pulmonary nodules is beneficial for the early detection of lung cancer. For the segmentation of small GGO pulmonary nodules, an integrated active contour model based on Markov random field energy and Bayesian probability difference (IACM_MRFEBPD) is proposed in this paper.

Methods: First, the Markov random field (MRF) is constructed on the computed tomography (CT) images, then the MRF energy is calculated. The MRF energy is used to construct the region term. It can not only enhance the contrast between pulmonary nodule and the background region, but also solve the problem of intensity inhomogeneity using local spatial correlation information between neighboring pixels in the image. Second, the Gaussian mixture model is used to establish the probability model of the image, and the model parameters are estimated by the expectation maximization (EM) algorithm. So the Bayesian posterior probability difference of each pixel can be calculated. The probability difference is used to construct the boundary detection term, which is 0 at the boundary. Therefore, the blurred boundary problem can be solved. Finally, under the framework of the level set, the integrated active contour model is constructed.

Results: To verify the effectiveness of the proposed method, the public data of the lung image database consortium and image database resource initiative (LIDC-IDRI) and the clinical data of the Affiliated Jiangmen Hospital of Sun Yat-sen University are used to perform experiments, and the intersection over union (IOU) score is used to evaluate the segmentation methods. Compared with other methods, the proposed method achieves the best results with the highest average IOU of 0.7444, 0.7503, and 0.7450 for LIDC-IDRI test set, clinical test set, and all test sets, respectively.

Conclusions: The experiment results show that the proposed method can segment various small GGO pulmonary nodules more accurately and robustly, which is helpful for the accurate evaluation of medical imaging.

Keywords: Small GGO pulmonary nodules, Image segmentation, Active contour model, MRF energy, Bayesian probability

Background

According to statistics, lung cancer has become the most common malignant tumor in the world, and it is also currently known as the cancer with the highest mortality after diagnosis [1]. The small ground glass opacity (GGO) pulmonary nodules are an early manifestation of lung cancer. Compared with solid pulmonary nodules, GGO pulmonary nodules have the characteristics of smaller diameter, lower contrast with surrounding normal lung tissue, intensity inhomogeneity, blurred boundary and irregular shape, which are often missed by doctors. Therefore, the detection and diagnosis of GGO pulmonary nodules have always been the focus and difficulty of imaging studies [2]. GGO pulmonary nodules are likely to become malignant tumors. If detected early, diagnosed early, and treated early, it will help reduce the risk of cancer [3]. In addition, small GGO pulmonary nodules are small size, and it is difficult to perform accurate puncture treatment at early stage. Therefore, multiple examinations are needed to pay close attention to their changes and evaluate them by medical imaging. The precise segmentation of GGO pulmonary nodules provides an important basis for medical imaging evaluation and diagnosis, so it has important clinical values.

At present, the segmentation methods of GGO pulmonary nodules mainly include mathematical morphology [4–6], active contour model [7, 8], and deep learning [9, 10]. The mathematical morphology method is based on set theory, and uses the structural elements of a given morphology to eliminate specific objects in the image. Kostis et al. [11] used the morphological algorithm with fixed size structural elements to distinguish small pulmonary nodules from surrounding vascular structures. Diciotti et al. [12] used mathematical morphological operations of corrosion and expansion to refine the segmentation results of pulmonary nodules. The active contour model method drives the curve or surface to deform by minimizing the energy function, thereby the target boundary can be reached. Farag et al. [13] proposed a level set-based pulmonary nodule segmentation algorithm to achieve adaptive segmentation of pulmonary nodules. Keshani et al. [14] used SVM classifier and active contour model to segment pulmonary nodules. Nithila et al. [8] used active contour model and fuzzy C-means clustering to segment pulmonary nodules. Li et al. [15] proposed an active contour based on adaptive local region energy function to segment GGO nodules. In recent years, deep learning method has been used to segment pulmonary nodules. Ye et al. [16] proposed a deep learning computer artificial intelligence system for early identification of GGO nodules. Roy et al. [17] proposed a collaborative combination of deep learning and shape-driven level set for automatic and accurate segmentation of pulmonary nodules. Wang et al. [18] proposed a central focus convolution neural network to segment pulmonary nodules. However, deep learning requires a large amount of labeled data, and it is still difficult to obtain a large number of pulmonary nodule labeled data. Most of the existing mathematical morphology and active contour model methods assume that the spatial location of each pixel in the image is statistically independent [19], which ignores the spatial structure information between pixels.

Markov random field (MRF) uses a neighborhood system to describe the relationship between neighboring pixels, which can well model the spatial structure information between pixels. Because of its small volume and easily affected by other factors such as blood vessels, pleura and surrounding highlight tissue, the segmentation of small

GGO pulmonary nodules is vulnerable to boundary leakage. Making full use of the spatial structure information between pixels will help solve this problem. It is worth noting that the MRF has been widely used in other fields such as prostate glands [20] and brain MR image segmentation [21]. But it is still rarely used in the segmentation of pulmonary nodules. Zhu et al. [22] proposed an MRF method based on simulated annealing algorithm (abbreviated as MRF_SA) for segmentation of GGO pulmonary nodules, which achieved good results. However, no comprehensive research has been conducted on various complex types of GGO pulmonary nodules. In addition, the blurred boundary problem is not considered in [22].

Based on the literature [22], we incorporate MRF energy into the region term of active contour model, and propose an integrated active contour model based on Markov random field energy and Bayesian probability difference (IACM_MRFEBPD). First, the K-means method is used to pre-segment the image to solve the sub-optimal problem of traditional MRF segmentation, which improves the segmentation efficiency. Based on this, MRF model is constructed. Labeling field and feature field are established, and MRF energy is calculated. Instead of the intensity information, the MRF energy is used for constructing the region term of the active contour model. The MRF prior of the labeling field and the Gaussian mixture model of the feature field are based on local statistical information of the image. So the intensity inhomogeneity can be solved. In addition, MRF energy can enhance the contrast of the pulmonary nodule and the background region. Therefore, the low contrast problem can be solved. Second, the probability model of GGO pulmonary nodules and surrounding background regions is constructed using the Gauss mixture model and the model parameters are estimated by the expectation maximization (EM) algorithm. Then, the Bayesian probability difference of each pixel is calculated and used as the boundary detection function of the active contour model. Probability difference is 0 at the boundary; thereby the blurred boundary problem can be effectively solved. Therefore, the proposed method can segment the small GGO pulmonary nodules with intensity inhomogeneity, low contrast and blurred boundary.

Results

Experimental data and evaluation indicator

To verify the effectiveness of the proposed method, we use the public data of the Lung Image Database Consortium and Image Database Resource Initiative (LIDC-IDRI) [23] and the clinical data of the Affiliated Jiangmen Hospital of Sun Yat-sen University to perform experiments. The public data contain 632 CT images, and the clinical data contain 32 CT images. So the experimental data total 664 CT images. The GGO lung nodules selected in all CT images are less than 15 mm in diameter, and most are less than 3 mm. To train the deep learning model, we divide all data into training and test sets. The training set contains 376 LIDC-IDRI CT images, and the test set contains 256 LIDC-IDRI and 32 clinical CT images. The identifier (ID) number of the LIDC-IDRI data is given in Table 4 (see "Appendix"), where XX–YY represents the YYth CT image of the XXth patient. Related parameters of CT images such as tube current and tube voltage can be easily found by the ID numbers.

The proposed method is compared with the other five methods, including literature [24] (abbreviated as LGDF), literature [25] (abbreviated as SFCM_LCM), literature

Table 1 IOU scores of LIDC-IDRI data

	CT image	LGDF	SFCM_LCM	LRBAC	MRF_SA	This paper	U-net
1	LIDC-IDRI-0759-000099	*0.7882*	0.5176	0.6941	0.7412	0.7412	0.6589
2	LIDC-IDRI-0294-000127	0.8289	0.4807	0.6558	0.6795	0.8373	*0.8567*
3	LIDC-IDRI-0743-000132	*0.9153*	0.5776	0.7931	0.8632	0.839	0.6348
4	LIDC-IDRI-0743-000201	*0.8678*	0.306	0.4181	0.6401	0.8021	0.7633
5	LIDC-IDRI-0400-000075	0.8841	0.5077	0.6769	0.8507	*0.9104*	0.7159
6	LIDC-IDRI-0375-000033	0.8343	0.3893	0.4765	0.6443	*0.8627*	0.715
Mean ± Std	All LIDC-IDRI test set	0.7217	0.4849	0.5692	0.6556	*0.7444*	0.6926

[26] (abbreviated as LRBAC), literature [22] (abbreviated as MRF_SA), and U-net model based on deep learning framework. The result manually segmented by radiologist is used as the gold standard. The pulmonary nodules less than 3 mm are located by LIDC-IDRI, but no gold standard is given. So most CT images have no gold standard. To solve this problem, we use the segmentation results of two radiologists in the Affiliated Jiangmen Hospital of Sun Yat-sen University as the gold standard. First, the two radiologists separately performed the segmentation, and then the combined results of the two people were used as the final gold standard.

In this paper, the intersection over union (IOU) score is used for evaluation indicator. The following is the calculation formula for IOU:

$$\mathrm{IOU} = \frac{|A_m \cap A_a|}{|A_m \cup A_a|} = \frac{\mathrm{TP}}{(\mathrm{TP} + \mathrm{FP} + \mathrm{FN})} \tag{1}$$

where A_m is the region segmented by experienced radiologist, A_a the region segmented by methods, TP the true-positive, FP the false-positive and FN the false-negative. The larger the IOU, the better the segmentation effect.

Model parameter setting

To set reasonable parameters for the proposed method, the comparative experiments are conducted on some important parameters. When calculating the MRF energy, the β (beta) in formula (6) has a certain effect on the experimental results. Figure 1 shows the segmentation results of LIDC-IDRI-0380-000037 when beta changes from 0.1 to 1.0. As can be seen from Fig. 1, when $\beta = 0.5$, the segmentation effect is the best. After multiple trials and comparisons, we choose $\beta = 0.5$ for the segmentation of all CT images. When calculating the Bayesian posterior probability difference, k in formula (10) determines whether the GGO with vascular adhesion and pleural adhesion, and the GGO surrounded with highlight tissue can be correctly segmented. Figure 2 shows the segmentation results of $k = 2$ and $k = 3$ in these three cases. As can be seen from Fig. 2, to correctly segment these three types of GGO, the value of k should be set to 3. λ_1, λ_2, μ and ν in formula (15) are set to 1 as the suggest in [27]. The selection of other parameters

will be discussed in "Methods" section. The parameter setting of the compared algorithm is consistent with the original literature.

The parameter settings of U-net are as follows: batch size: 10, learning rate: 0.0001, loss function: binary cross-entropy. The segmentation result of the U-net method is related to the iteration number. Figure 3 shows the average IOU value of LIDC-IDRI test set, clinical test set, and the entire test set when the iteration number changes from 150 to 500. When the iteration number is 200, the average IOU value is the largest. So the iteration number of the U-net method is set to 200.

Segmented results of LIDC-IDRI data

Figure 4 shows the segmented results of 6 images with 6 methods. Figure 4a is the original image, and Fig. 4b is the segmented result by radiologist, which is the gold standard. Segmented results marked with red box are obtained by the proposed method. In the first image, the pulmonary nodule had mild vascular adhesion and the nodule was close to the pleura. The LGDF method (Fig. 4c) incorrectly segmented some of the blood vessels and a boundary leakage occurred at the pleura. Both the SFCM_LCM method (Fig. 4d) and the MRF_SA method (Fig. 4f) produced boundary leakage at the pleura. The U-net method (Fig. 4h) incorrectly segmented some of the blood vessels. Segmented results of the LRBAC method (Fig. 4e) are comparable to the proposed method. In the second image, the pulmonary nodule was relatively close to the pleura. Except that the proposed method can correctly segment, the U-net method mistakenly segmented some lung parenchyma and other algorithms produced the boundary leakage at the pleura. In the third image, the pulmonary nodule was relatively isolated but intensity inhomogeneity, and the shape was irregular. The SFCM_LCM method cannot correctly identify the shape of the pulmonary nodule; other methods worked comparable intuitively, but the U-net method mistakenly segmented some lung parenchyma. In the fourth image, the shape of the pulmonary nodule was extremely irregular, and with vascular adhesions. The proposed method and U-net correctly segmented, while other methods segmented some blood vessels. At the same time, other methods produced different degrees of under-segmentation due to blurred boundary. In the fifth image, the pulmonary nodule

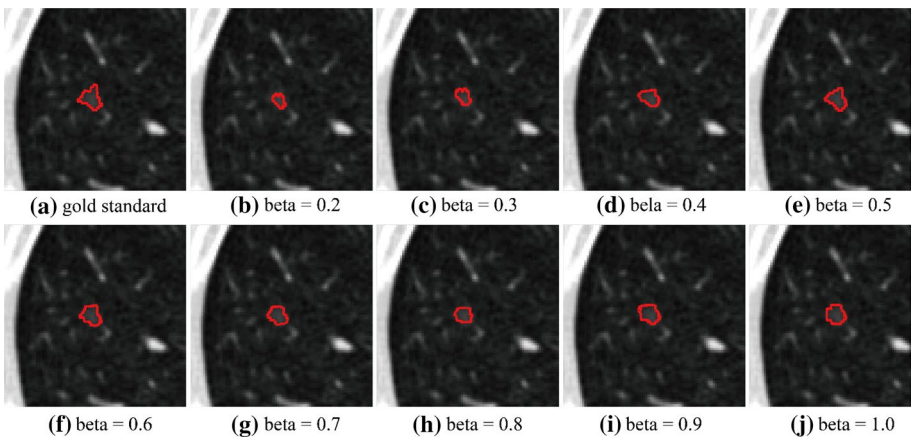

Fig. 1 Segmented results with different beta values

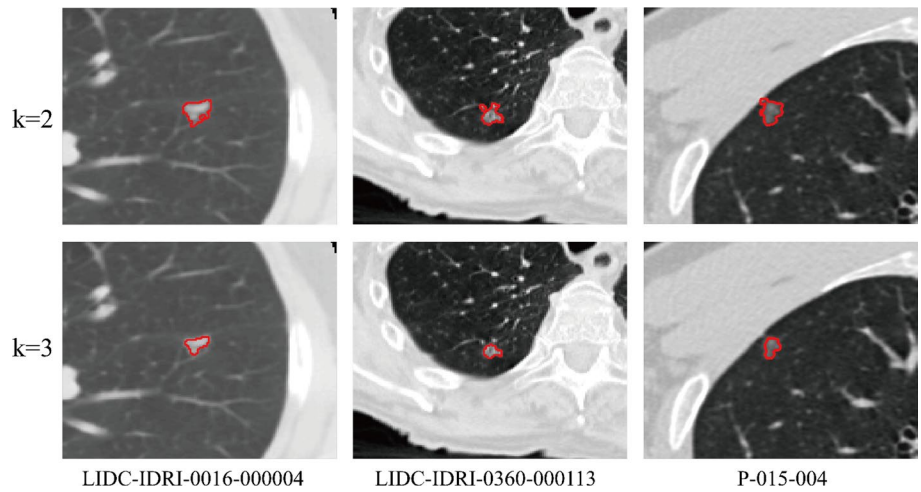

Fig. 2 Segmented results with different *k* values

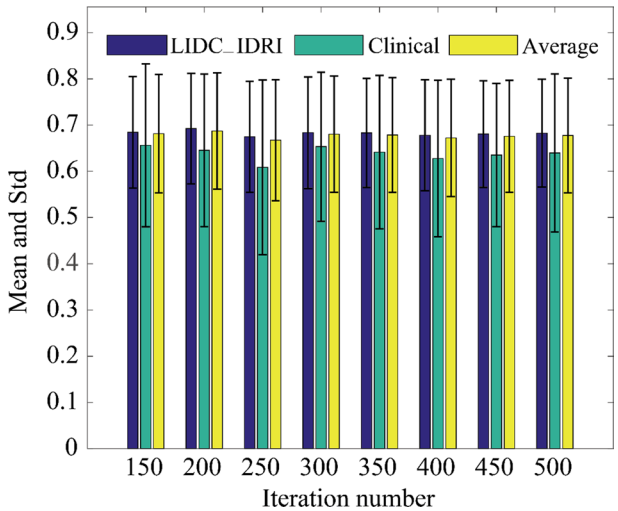

Fig. 3 Average IOU with different iteration number

was relatively small, and with low contrast. The proposed method achieved better segmentation effect, while other methods produced under-segmentation, and the SFCM_LCM method was more serious. In the sixth image, boundary of the pulmonary nodule was blurred, and the boundary over-band was relatively large. In addition, the shape was irregular. The proposed method achieved a better segmentation effect and the U-net produced a certain over-segmentation, while other methods produced different degrees of under-segmentation, and the segmented boundary shrunk toward the interior of the pulmonary nodule.

In summary, the segmented boundary of the SFCM_LCM method is severely inwardly contracted and the shape of the pulmonary nodule cannot be identified. The proposed method has achieved better segmentation results, followed by the LRBAC method.

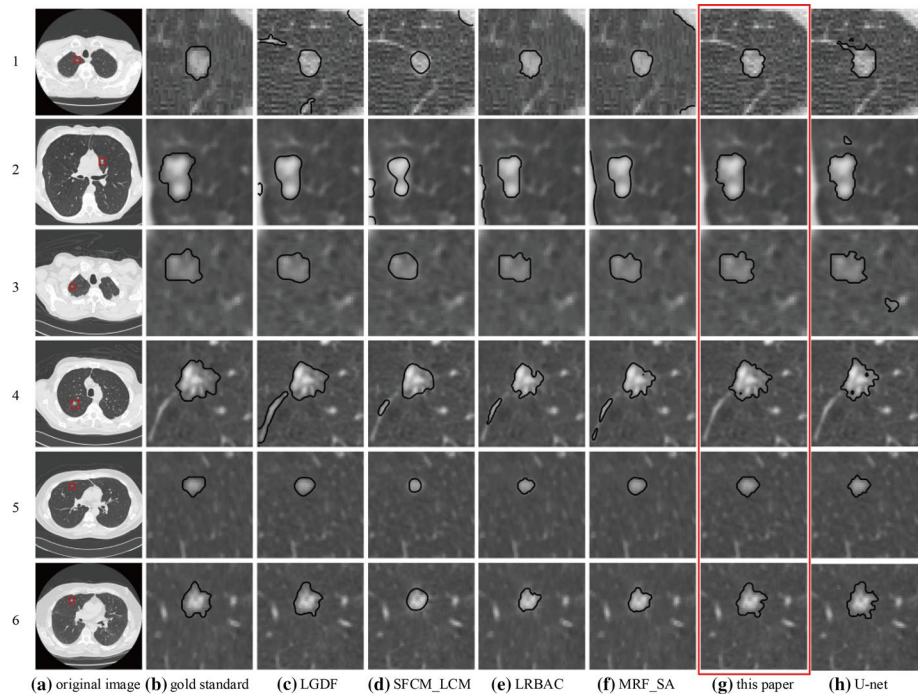

Fig. 4 Segmented results of LIDC-IDRI data

To better evaluate the performance of various methods, Table 1 gives the IOU scores for 6 LIDC-IDRI CT images in Fig. 4 and the average IOU for LIDC-IDRI test set. In addition, Table 1 shows the ID numbers of 6 CT images in Fig. 4. The optimal IOU score is highlighted in boldface. It can be seen from table that the proposed method achieved the best results, followed by LGDF. The effect of SFCM_LCM is the worst; the main reason is that there exists serious under-segmentation.

Segmented results of clinical data

Figure 5 shows the segmented results of 8 images with 6 methods. Figure 5a is the original image, and Fig. 5b is the segmented result by radiologist. Segmented results marked with red box are obtained by the proposed method. In the first three images, the pulmonary nodules were isolated, and with low contrast. Intuitively, all methods achieved the same effect, but the SFCM_LCM method produced a certain boundary leakage, and the segmented boundary shrunk inward. In the fourth image, blood vessel adhesion around the pulmonary nodule was relatively serious. The proposed method achieved good results, but other methods produced boundary leakage. In the fifth image, the pulmonary nodule was heavily adhered to the pleura and surrounded by blood vessels and other highlight tissues. Except for the proposed method, other methods all produced boundary leakage. In addition, the U-net produced serious under-segmentation. In the sixth image, the pulmonary nodule was close to the surrounding highlight tissue. Except for the SFCM_LCM method and the proposed method, other methods all produced boundary leakage, but the segmented boundary of SFCM_LCM method shrunk to the

Table 2 IOU scores of clinical data

	CT image	LGDF	SFCM_LCM	LRBAC	MRF_SA	This paper	U-net
1	P-001-001	0.7537	0.6784	0.7753	0.7453	0.5874	*0.8078*
2	P-002-025	*0.9253*	0.8375	0.9167	0.888	0.9205	0.7917
3	P-003-122	*0.8661*	0.6546	0.8314	0.8367	0.8392	0.8007
4	P-004-072	0.3525	0.6267	0.4153	0.3136	*0.6379*	0.2582
5	P-005-035	*0.7993*	*0.7993*	0.3152	0.3316	0.7964	0.3991
6	P-006-024	0.6705	*0.7703*	0.6627	0.6061	0.6403	0.6429
7	P-007-001	*0.9048*	0.7561	*0.9048*	*0.9048*	0.7619	0.375
8	P-008-029	*0.8623*	0.8136	0.7412	0.5339	0.7221	0.7706
Mean ± Std	All clinical test set	0.707	0.6057	0.5602	0.6456	*0.7503*	0.6453

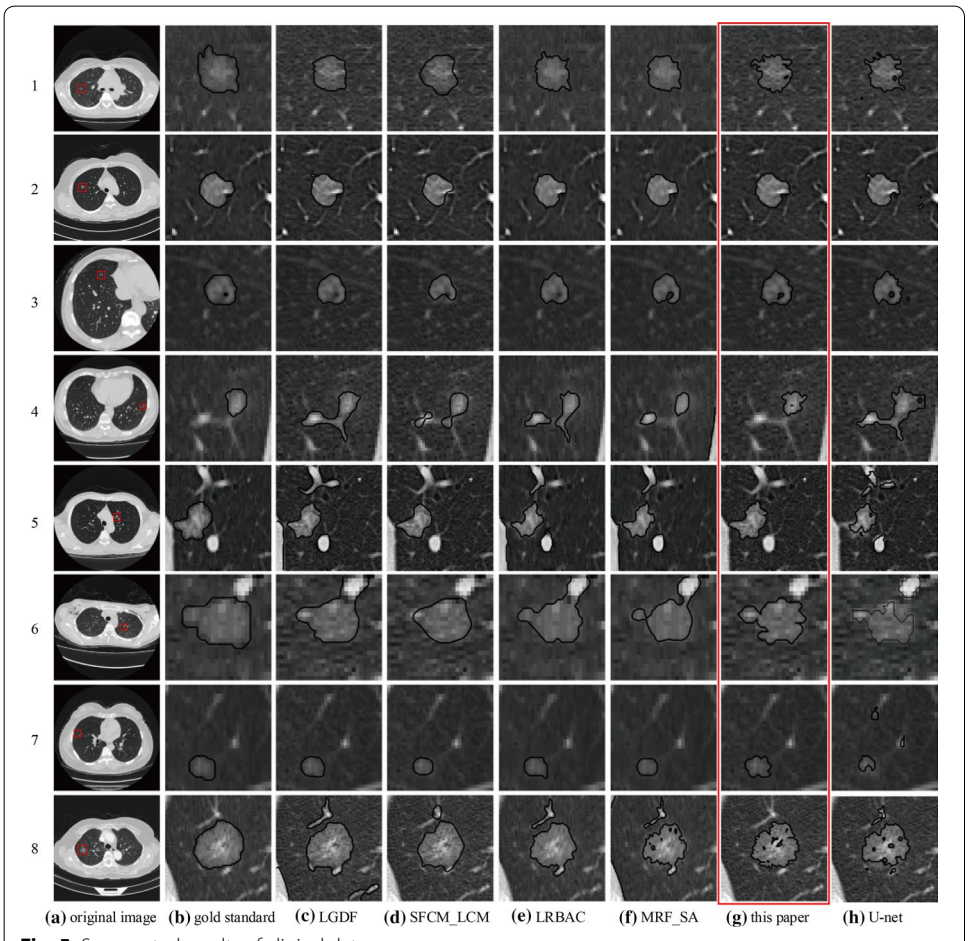

Fig. 5 Segmented results of clinical data

internal of the pulmonary nodule. In the seventh image, the pulmonary nodule was isolated, and with low contrast and small size. Except for the U-net method, other methods can segment the pulmonary nodule, but the segmented boundaries had different degrees of leakage, and the segmented boundary shrunk to the inside of the pulmonary nodule. In the eighth image, the pulmonary nodule was relatively large, but with intensity inhomogeneity, and there are many dark spots inside, which may be caused by bubbles or necrotic tissue. Furthermore, there are blood vessels adjacent to the nodules but not

connected. Except for our method, other methods produced boundary leakage, and surrounding blood vessels were segmented. It is worth noting that the two methods based on MRF (MRF_SA and the proposed method) can correctly identify and segment the dark spots in the pulmonary nodule. It may be that the MRF effectively utilizes the spatial structure information of the image.

In the segmentation results of these 8 clinical CT images, the U-net effect is not good, with serious boundary leakage and under-segmentation.

Table 2 shows the IOU scores of 8 clinical CT images in Fig. 5 and the average IOU for clinical test set. It can be seen that the proposed method achieved better segmentation results with the highest average IOU, followed by LGDF. Although the proposed method has no obvious advantages in the segmentation results of a single CT image, it is stable in the segmentation results of multiple CT images. The IOU scores of other methods are very high for some CT images, but are very low in some case. In summary, the proposed method has good robustness.

Table 3 shows the average IOU of LIDC-IDRI data, clinical data, and all test sets. The proposed methods all achieved the highest average IOU, followed by LGDF.

Discussion

Based on the above-segmented results of LIDC data and clinical data, the proposed method has achieved better segmented results. In the segmentation experiments of clinical data, all methods have different degrees of boundary leakage, which are due to the influence of various factors such as blood vessels, pleura, and surrounding highlight tissue, etc. Therefore, the segmentation of small GGO pulmonary nodules is still very challenging.

LGDF method [24] uses Gaussian distributions with different mean and variance to describe local intensity information of the image, and uses truncated Gaussian kernel to define local attributes. The mean and variance of local intensity are considered as a function of spatial variation to deal with intensity inhomogeneity and spatially varying noise. However, the performance of the LGDF method depends more on the value of the local window size. When the value is not appropriate, the kernel function cannot be significantly reduced to zero. So it will cause boundary leakage. This phenomenon is particularly evident in the experiments of clinical data. In addition, the low contrast and blurred boundary are also the cause of the boundary leakage.

SFCM_LCM method [25] uses a spatially constrained fuzzy clustering method for the initialization and parameter control of the level set function, which promotes the evolution of the level set and improves the robustness of segmentation. At the same time, a local regular term is introduced to solve the problem of intensity inhomogeneity. However, the fuzzy nature of SFCM_LCM makes it impossible to correctly recognize

Table 3 Average IOU scores of LIDC_IDRI test set, clinical test set and all test sets

	CT image	LGDF	SFCM_LCM	LRBAC	MRF_SA	This paper	U-net
1	LIDC_IDRI test set	0.7217	0.4849	0.5692	0.6556	*0.7444*	0.6926
2	Clinical test set	0.707	0.6057	0.5602	0.6456	*0.7503*	0.6453
3	All test set	0.7201	0.4983	0.5682	0.6545	*0.745*	0.6873

the shape of pulmonary nodules. Therefore, for irregularly shaped pulmonary nodules, SFCM_LCM segmentation results are relatively poor.

LRBAC method [26] is a very effective local segmentation method, which increases the segmentation ability of intensity inhomogeneity images by introducing local statistical information. However, to achieve narrow-band control, the level set function in LRBAC needs to be re-initialized as a symbol distance function every few iterations during the process of model solving, and the calculation cost is high. At the same time, errors in the re-initialization process will cause the narrow-band control to be unstable, which affects the stability and robustness of the segmentation results. In addition, experiments have found that the segmentation results of LRBAC are sensitive to the selection of the local domain radius. If the local radius is too small, the segmentation may be insufficient, and if the local radius is too large, the segmentation may be excessive. In the actual pulmonary nodule segmentation, it is difficult to set a separate local radius for each segmentation. Finally, it should be noted that, compared with the global segmentation method, the local segmentation method is usually more sensitive to the initial contour. Therefore, the initial contour greatly affects the segmentation results of LRBAC.

Compared with MRF_SA method [22] and other MRF-based methods, the proposed method has two differences. First, the initial segmentation is helpful for the optimization of the MRF, and prevents the calculation from being stopped if it falls into a local minimum. Second, the MRF energy is calculated only once, and the MRF energy of each pixel no longer changes during the evolution of the contour. Unlike other MRF methods, this paper aims to use MRF energy to enhance the contrast of pulmonary nodules and background regions, rather than calculating the optimal solution of MRF in the framework of active contour models [21].

There are three main reasons why the proposed method has achieved good segmentation results. First, Markov's prior is equivalent to performing a probabilistic morphological closing operation on the image, making spatially adjacent pixels more inclined to the same region, reducing the possibility of suspicious boundaries caused by noise and other tissues, such as blood vessels. Second, MRF energy calculation makes full use of the spatial structure information between pixels, which can enhance the contrast between pulmonary nodules and the background regions. So the problem of low contrast can be solved. At the same time, it is assumed that each pixel in the image conforms to a Gaussian mixture distribution when modeling the MRF feature field and this will make full use of local statistical information, which is helpful to solve the problem of intensity inhomogeneity. Third, the Bayesian probability difference is used for constructing boundary detection term. Probability difference is 0 at the segmentation boundary, which can well solve the blurred boundary problem. So the proposed method can deal with GGO pulmonary nodules with low contrast, intensity inhomogeneity and blurred boundary.

Finally, based on Bayesian posterior probability and initial segmentation by K-means method, the initial contour of the curve evolution can be obtained. Since the initial contour is located near the target boundary of image segmentation, the curve evolution can obtain the global minimum energy, which improves the stability and robustness of the proposed method. In the future work, we will continue to optimize the solution of the proposed model [28, 29].

Conclusion

An integrated active contour model based on MRF energy and Bayesian probability difference is proposed in this paper. First, the MRF is constructed on the CT images and MRF energy is calculated. Instead of the intensity information, the MRF energy is used for constructing the region term. Second, the Gaussian mixture model is used to establish the probability model of pulmonary nodule image and the Bayesian posterior probability difference of each pixel is calculated. Next, the probability difference is used for constructing the boundary detection term. Finally, under the framework of the level set, the integrated active contour model is constructed. The experimental results of LIDC-IDRI data and clinical data show that the proposed method can segment various types of GGO pulmonary nodules more accurately and robustly than other methods. However, the proposed method does not specifically test for a certain type of GGO pulmonary nodules (such as GGO pulmonary nodules with different degrees of vascular adhesion) with a large number of samples, the robustness, stability and reliability of the proposed method need to be further verified. In the future work, when segmenting GGO pulmonary nodules with different degrees of vascular adhesion, we can combine MRF with shape information to accurately segment pulmonary nodules and blood vessels.

Methods

Assuming that C is a closed contour curve, the image region Ω is divided into region Ω_1 and Ω_2 by the curve, where Ω_1 represents the interior of the curve and Ω_2 represents the exterior of the curve. MRF energy instead of intensity information is used for constructing region term, which drives the curve to move to the target boundary. Bayesian probability difference instead of gradient information is used for constructing boundary detection term. The probability difference is 0 at the boundary, which stops the curve from evolving. Therefore, the energy function of the integrated active contour model can be defined as

$$E(\phi, C) = \lambda E_R(\phi) + \mu E_E(C) \tag{2}$$

where $E_R(\phi)$ is the region term, $E_E(C)$ is the boundary detection term, μ and λ are two parameters that control the region term and the boundary detection term, respectively, and ϕ is the level set function. Figure 6 shows the image segmentation process of the integrated active contour model. The construction of region term and boundary detection term will be discussed later.

Construction of the region term based on MRF energy

Traditional MRF is solved by multiple iterations, which is easy to fall into local optimum solution during the iterative process. The initial segmentation of the image can make the initial boundary near the real boundary, which improves the efficiency and stability of optimization solution, and effectively avoids the local optimal situation. Therefore, the initial segmentation can improve the accuracy and robustness of segmentation. In this paper, the K-Means algorithm is used to perform the initial segmentation of the original image, and then the MRF is constructed.

The image can be regarded as a two-dimensional MRF, whose pixel values are only related to its neighboring pixels. Assuming that the image size is $M * N$, the set of pixels

in the image is represented by S, and $S = \{s(i,j)|1 \le i \le M, 1 \le j \le N\}$. Each element s in the set S is represented by neighborhood system. The potential clique c is a subset of S, in which c can be expressed as single-point potential clique, double-point potential clique and three-point potential clique, etc. As the order of the neighborhood system increases, the number of potential cliques will increase rapidly. Next, the MRF energy will be calculated using the neighborhood system and potential energy function.

First, constructing an MRF requires the construction of two fields, that is, labeling field and feature field. The labeling field is used to classify the image to be segmented, and the feature field is used to perform feature analysis on the classified region. The labeling field is represented by X, and $X = \{x_s, s \in S\}$. The labeling field value of any pixel is represented by x_s. The labeling space is represented by $\Lambda = \{1, 2, \ldots, L\}$, which divides the image into L regions and Λ is the set of random variables x_s, so $x_s \in \Lambda$ [22]. The feature field (or observation field) is represented by Y, and $Y = \{y_s, s \in S\}$. The feature field value of any pixel is represented by y_s. According to the Bayesian theory, the maximum posteriori probability can be expressed as

$$\hat{X} = \arg\max_x P(X|Y) = \arg\max_x \frac{P(X)P(Y|X)}{P(Y)} \tag{3}$$

where Y is the observed image, so it can be regarded as a constant, which has no effect on maximizing the posterior probability. Therefore, the above formula can be written as follows:

$$\hat{X} = \arg\max_x P(X|Y) \propto \arg\max_x P(X)P(Y|X). \tag{4}$$

$P(X)$ is called segmentation model, which is modeled as MRF prior. It will be seen that $P(X)$ is a Gibbs distribution. Conditional probability $P(Y|X)$ is a data model, usually a Gaussian distribution; that is to say, the distribution of pixel value obeys Gaussian distribution after given label category [22]. To better fit the distribution of the pixel values, a mixed Gauss distribution is used for $P(Y|X)$ in this paper. In the following, we will model the labeling field (segmentation model $P(X)$) and the feature field (data model $P(Y|X)$), respectively.

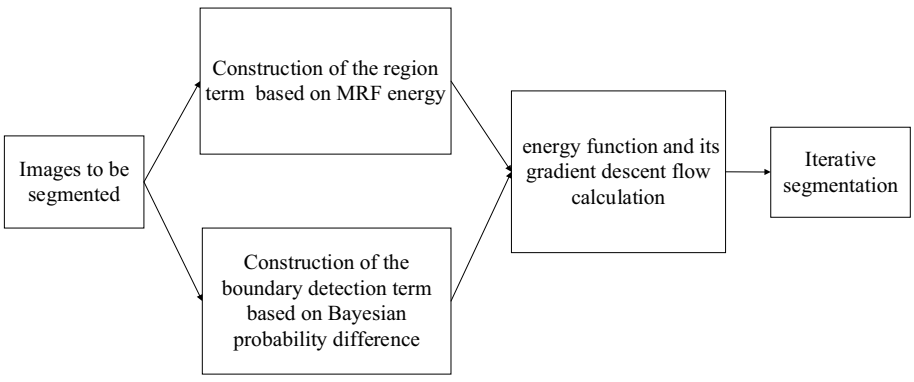

Fig. 6 Image segmentation process

By Hammersley–Clifford theorem, the prior probability $P(X)$ can be obtained [30], that is

$$P(X) = \prod_{s\in S} P(x_s) = \prod_{s\in S} \frac{\exp\left[-\sum_{c\in C} V_c(x_s)\right]}{\sum_{x_s=1}^{L} \exp\left[-\sum_{c\in C} V_c(x_s)\right]}, \tag{5}$$

where $V_c(x_s)$ is the potential function of the potential clique c containing x_s, and all potential clique set is represented by C. There are many ways to model $V_c(x_s)$ (labeling field modeling), such as Ising model, Potts model, MLL model, etc. In this paper, we use Potts model, which is consistent with literature [22]. The Potts model only considers the binary potential function, which is defined as

$$V_c(x_s) = V_2(x_i, x_j) = \begin{cases} 0 & x_i = x_j \\ \beta & x_i \neq x_j \end{cases}. \tag{6}$$

Next, the second-order neighborhood system is used and the corresponding potential cliques are two-point. β denotes the parameter of the two-point potential clique, usually between 0.5 and 1.0. In our experiment, β is set to 0.5.

Assuming that each pixel of the image obeys the independent and identical distribution, also obeys the Gauss mixture distribution. The conditional distribution of the feature field under a given labeling field is given as follows:

$$P(Y|X) = \prod_{s\in S} P(y_S|x_S) = \prod_{s\in S} \frac{1}{\sqrt{2\pi}\sigma_m} \exp\left[-\frac{(y_s-\mu_m)^2}{2\sigma_m^2}\right]. \tag{7}$$

The parameters μ_m and σ_m are the mean and variance of the mth target region, respectively. In our experiment, m is set to 2, which is consistent with the literature [19].

Substituting (5) and (7) into (4), and taking logarithms on both sides of (4), we can get

$$\begin{aligned} \hat{X} &= \arg\max_x (\ln P(X) + \ln P(Y|X)) \\ &= \arg\max_x \left\{ -\sum_{c\in C} V_c(x_s) - \left[\sum_{s\in S}\left(\ln(\sqrt{2\pi}\sigma_m) + \frac{(y_s-\mu_m)^2}{2\sigma_m^2}\right)\right]\right\} \\ &= \arg\min_x \left\{ \sum_{c\in C} V_c(x_s) + \left[\sum_{s\in S}\left(\ln(\sqrt{2\pi}\sigma_m) + \frac{(y_s-\mu_m)^2}{2\sigma_m^2}\right)\right]\right\} \\ &= \arg\min_x (U_1(X,Y) + U_2(X)) \end{aligned} \tag{8}$$

where $U_1(X,Y) = \ln P(Y|X) = \sum_{s\in S}\left(\ln(\sqrt{2\pi}\sigma_m) + \frac{(y_s-\mu_m)^2}{2\sigma_m^2}\right)$, $U_2(X) = \sum_{c\in C} V_c(x_s)$; $U_1(X,Y)$ is conditional energy function (i.e., feature field energy), $U_2(X)$ is prior energy function (i.e., labeling field energy), $U(X,Y) = U_1(X,Y) + U_2(X)$ is MRF energy.

In summary, the calculation steps of MRF energy can be obtained as follows:

1. K-Means algorithm is used to initial segmentation, where $K=3$, we divide the lung parenchyma, lung nodules and other lung tissue (blood vessels, pleura and highlight tissue, etc.) into three categories;

2. Solving the parameters (mean μ_m and variance σ_m) of the Gaussian mixture model using the expectation maximization method;
3. The total MRF energy $U(X, Y)$ is obtained from Eq. (8).

The MRF energy $U(X, Y)$ of each pixel can be calculated by (8). For the convenience of distinguishing and discussing later, the $U(X, Y)$ energy matrix is flattened into one-dimensional vector $u(x)$, where $1 \leq x \leq M * N$ represents the coordinate position of each pixel. MRF energy instead of intensity information is used for constructing region term of active contour model [31]; the region term can be constructed as follows:

$$E_R(\phi) = \sum_{i=1,2} \int_{\Omega} \left(u(x) - f_i(x)\right)^2 M_i(\phi) \mathrm{d}x \tag{9}$$

$f_1(x)$ and $f_2(x)$ are the mean values of MRF energy inside and outside of the contour curve, respectively. $M_1(\phi) = H(\phi)$ represents the inside of the curve, and $M_2(\phi) = 1 - H(\phi)$ represents the outside of the curve, where $H(\phi)$ is Heaviside function, $H(\phi) = \frac{1}{2}\left(1 + \frac{2}{\pi} \arctan \frac{\phi}{\varepsilon}\right)$.

It can be seen intuitively from Fig. 7 that MRF energy can significantly enhance the contrast between small GGO pulmonary nodule and background region. To further confirm the contrast enhancement effect, the intensity values and MRF energy values of pulmonary nodule and background region were compared and analyzed. Figure 7a is a CT image of a patient, the region drawn in the box is where the pulmonary nodule is located at. Figure 7b, c shows the intensity image and energy image of the region that is drawn in the box, respectively. Box 1 and 2 in Fig. 7b represents the pulmonary nodule region (segmented region) and the pulmonary parenchyma region (background region), respectively. Box 3 and 4 in Fig. 7c is similar. Figure 7d, e shows the intensity values corresponding to box 1 and 2, respectively, and Fig. 7f, g shows the energy values corresponding to box 3 and 4, respectively. Comparing the intensity value of box 1 (Fig. 7d) and the energy values of box 3 (Fig. 7e), it can be found that the energy values of the pulmonary nodule are significantly increased. Comparing the intensity values of box 2 (Fig. 7f) and the energy values of box 4 (Fig. 7g), it can be found that the energy values of the pulmonary parenchyma are reduced. Therefore, MRF energy can significantly enhance the contrast between pulmonary nodule and pulmonary parenchyma. In addition, the conditional probability $P(Y|X)$ is selected as the Gaussian mixture distribution when modeling the feature field of MRF. It effectively utilizes the local statistical information, which can reduce the suspicious boundary caused by factors such as intensity inhomogeneity and noise.

Construction of the boundary detection term based on Bayesian probability difference

Assuming that the intensity of image pixels obeys the Gaussian mixture model (GMM) distribution [32], the specific form is a linear combination of Gaussian distributions:

$$p(x) = \sum_{k=1}^{K} \alpha_k N(x|\mu_k, \Sigma_k) \tag{10}$$

where μ_k and Σ_k represent the mean and variance of the kth Gaussian distribution, respectively. α_k represents the coefficients of the Gaussian mixture term, and $0 \leq \alpha_k \leq 1$, $\sum_{k=1}^{K} \alpha_k = 1$.

$X = \{x_1, x_2, \ldots, x_n\}$ denotes a dataset consisting of n pixels of an image, $Z = \{z_1, z_2, \ldots, z_n\}$ is a dataset consisting of n implicit data (i.e., implicit variables), and $\theta = \{\alpha_k, \mu_k, \Sigma_k | k = 1, 2, \ldots, K\}$ is the parameters of Gaussian mixture distribution. The optimal parameter θ can be obtained by solving the maximum of logarithmic likelihood function. The likelihood function is as follows:

$$L(\theta) = \ln p(X|\theta) = \ln \sum_{z} p(X, Z|\theta). \tag{11}$$

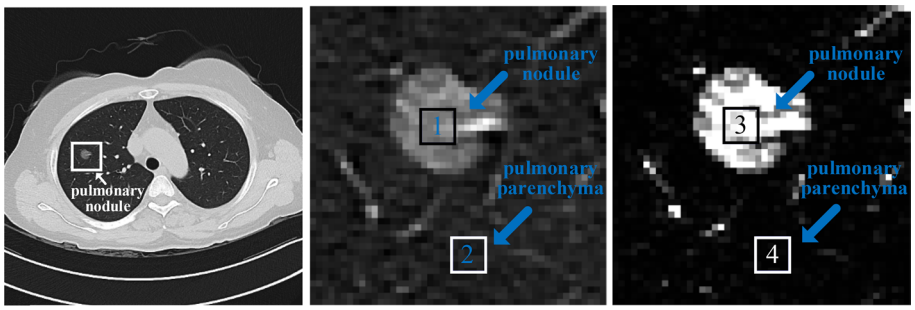

(a) CT image of pulmonary nodule **(b)** Intensity image **(c)** Energy image

119	129	129	123	109	99
131	116	110	112	117	118
139	122	111	111	119	136
113	109	116	134	144	149
119	114	114	115	131	132
125	111	105	97	104	114

(d) Box 1 intensity value

50	43	46	43	43	56
49	42	37	47	41	48
42	56	46	38	38	48
47	54	54	56	55	54
37	48	52	53	50	48
39	45	36	36	48	42

(e) Box 2 intensity value

255	255	255	255	207	151
255	251	213	225	255	255
255	255	219	219	255	255
232	207	251	255	255	255
255	238	238	245	255	255
255	219	183	141	178	238

(f) Box 3 energy value

27	29	27	29	29	29
27	29	35	27	30	27
29	29	27	33	33	27
27	28	28	29	28	28
35	27	27	27	27	27
32	28	36	36	27	29

(g) Box 4 energy value

Fig. 7 Contrast enhancement by MRF energy

The above formula can be solved effectively by EM algorithm [33], and then the optimal parameter set θ can be obtained. Further, $p_k(x_i|\theta_k)$ can be obtained by θ, which represents the kth Gaussian component. For sample x_i, $p(k|x_i,\theta)$ is the posterior probability of the k th Gaussian component, which is defined as follows:

$$p(k|x_i,\theta) = \frac{\alpha_k p_k(x_i|\theta_k)}{\sum_{k=1}^{K} \alpha_k p_k(x_i|\theta_k)}. \tag{12}$$

Therefore, for any pixel x, the Bayesian posterior probability of the pixel x that belonging to the pulmonary nodule class can be calculated, denoted as $p(1|x,\theta)$. Similarly, the Bayesian posterior probability of the pixel x that belonging to the background region class can be calculated, denoted as $p(2|x,\theta)$. Thus, the boundary stopping function based on Bayesian probability difference can be obtained as follows:

$$S = |p(1|x,\theta) - p(2|x,\theta)|. \tag{13}$$

According to the edge-based active contour model [34], the boundary detection terms can be constructed as follows:

$$E_E(\mathrm{C}) = \oint_C g(|\nabla I(C(s))|)\mathrm{d}s = \oint_C S\mathrm{d}s = \int_\Omega S\delta(\phi)|\nabla\phi|\mathrm{d}x. \tag{14}$$

Figure 8 is an effect diagram of the boundary detection function based on Bayesian probability difference. Figure 8a is a CT image of a patient, the region drawn in the box is where the pulmonary nodule is located at, and the pulmonary nodule has a blurred boundary. Figure 8b is an enlarged image of the region drawn in the box, A–B line segment passes through the pulmonary nodule, point A is the left boundary, and B is the right boundary. The X and Y coordinates of points A and B in the image are (20, 19) and (20, 33), respectively. Figure 8c is an intensity graph of pixels on the C–D line segment. Figure 8d is a Bayesian probability difference graph of pixels on the C–D line segment. As we can be seen from Fig. 8, the Bayesian probability difference on points A and B is 0, so the probability difference can effectively detect the blurred boundary of the pulmonary nodule. The intensity values of points A and B did not change significantly, so the gradient calculated by the intensity values would not change much. Therefore, the blurred boundary of the GGO pulmonary nodule cannot be effectively detected by the gradient information.

Construction and solution of energy function

The final energy function of the integrated active contour model can be obtained by substituting (9) and (14) into (2), specifically as follows:

$$
\begin{aligned}
E(\phi) = \lambda_1 \int_{\Omega} \big(u(x) - f_1(x)\big)^2 H(\phi)\mathrm{d}x \\
+ \lambda_2 \int_{\Omega} \big(u(x) - f_2(x)\big)^2 (1 - H(\phi))\mathrm{d}x \\
+ \mu \int_{\Omega} S\delta(\phi)|\nabla\phi|\mathrm{d}x + \nu \int_{\Omega} \frac{1}{2}(|\nabla\phi| - 1)^2 \mathrm{d}x.
\end{aligned} \tag{15}
$$

At the right of (15), the first two terms are region term, the third one is boundary detection term, and the fourth one is the regular term which guarantees that the level set function ϕ is kept as the symbolic distance function [35], i.e., guaranteeing that $|\nabla\phi| = 1$. $u(x)$ is defined by (9), and S is defined by (13). Next, we will solve the energy function.

First, level set function ϕ is fixed. Taking the partial derivative of the energy functional $E(\phi)$ with respect to $f_1(x)$ and $f_2(x)$, respectively, and making them equal to zero, we can get that

$$
f_1(x) = \frac{\int_{\Omega} u(x)H(\phi)\mathrm{d}x}{\int_{\Omega} H(\phi)\mathrm{d}x}, \quad f_2(x) = \frac{\int_{\Omega} u(x)(1 - H(\phi))\mathrm{d}x}{\int_{\Omega} (1 - H(\phi))\mathrm{d}x}. \tag{16}
$$

Second, $f_1(x)$ and $f_2(x)$ are fixed. Taking the derivative of the energy functional $E(\phi)$ with respect to ϕ, ϕ is solved by gradient descending flow, details as follows:

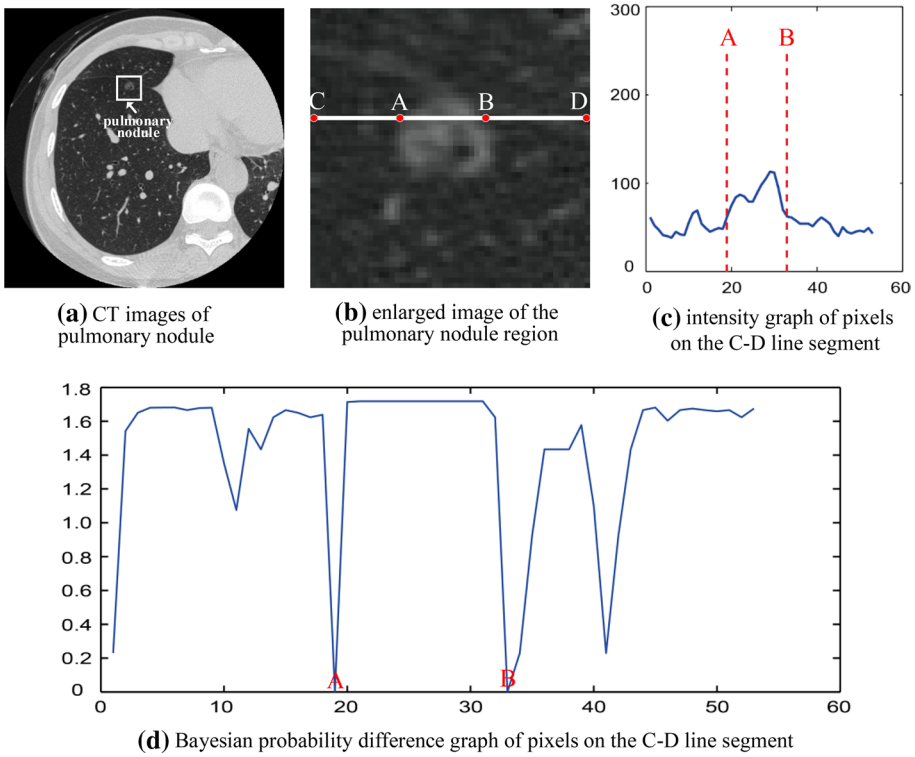

(a) CT images of pulmonary nodule

(b) enlarged image of the pulmonary nodule region

(c) intensity graph of pixels on the C-D line segment

(d) Bayesian probability difference graph of pixels on the C-D line segment

Fig. 8 Boundary detection based on Bayesian probability difference

$$\frac{\partial \phi}{\partial t} = \lambda \cdot \delta(\phi)\left(\left(u(x) - f_2(x)\right)^2 - \left(u(x) - f_1(x)\right)^2\right) + \mu \cdot \delta(\phi) div\left(S\frac{\nabla \phi}{|\nabla \phi|}\right) + v \cdot \left(\nabla^2 \phi - div\left(\frac{\nabla \phi}{|\nabla \phi|}\right)\right) \tag{17}$$

where $\delta(\phi) = \frac{\varepsilon}{\pi}\frac{1}{\varepsilon^2+\phi^2}$ is the derivative of $H(\phi)$, also known as the Dirac Delta function.

Abbreviations

CAD: Computer-aided diagnosis; GGO: Ground glass opacity; IACM_MRFEBPD: Integrated active contour model based on Markov random field energy and Bayesian probability difference; MRF: Markov random field; CT: Computed tomography; EM: Expectation maximization; LIDC-IDRI: Lung image database consortium and image database resource initiative; IOU: Intersection over union; ID: Identifier; GMM: Gaussian mixture model; LGDF: Local Gaussian distribution fitting energy; SFCM_LCM: Spatial fuzzy clustering with level set methods; LRBAC: Localizing region-based active contours; MRF_SA: Markov random field with simulated annealing algorithm.

Acknowledgements

Not applicable.

Authors' contributions

SZ and ZZ contributed to the study concept and design. YC and BF were involved in the acquisition of data. XC and WL conducted the analysis and interpretation of data. SZ and ZZ worked on the preparation of the manuscript. All authors read and approved the final manuscript.

Funding

This work is supported by National Natural Science Foundation of China (Nos. 61967004, 11901137, and 81960324), Natural Science Foundation of Guangxi Province (Nos. 2018GXNSFBA281023 and 2016GXNSFBA380160), Guangxi Key Laboratory of Automatic Testing Technology and Instruments (Nos. YQ20113, YQ19209, and YQ18107); Guangxi Key Laboratory of Cryptography and Information Security (Nos. GCIS201927); Innovation Project of Guet Graduate Education (No. 2019YCXB03).

Availability of data and materials

The datasets used and/or analyzed during the current study are available from the corresponding author on reasonable request.

Ethics approval and consent to participate

This study was approved by the ethics committee of the Affiliated Jiangmen Hospital of Sun Yat-sen University.

Consent for publication

Not applicable.

Competing interests

The authors declare that they have no competing interests.

Author details

[1] School of Electronic Engineering and Automation, Guilin University of Electronic Technology, Guilin 541004, China. [2] School of Mathematics and Computational Science, Guilin University of Electronic Technology, Guilin 541004, China. [3] School of Electronic Information and Automation, Guilin University of Aerospace Technology, Guilin 541004, China. [4] The Department of Radiology, The Affiliated Jiangmen Hospital of Sun Yat-sen University, Jiangmen 529000, China.

Appendix

Table 4 gives the ID numbers of all data in LIDC-IDRI. The meaning of the numerical sequence in the table has been explained in the experimental data description section.

Table 4 ID numbers of LIDC-IDRI data

Training set	Training set	Training set	Training set	Training set	Test set	Test set	Test set	Test set
0001-000128	0045-000042	0088-000079	0340-000259	0398-000129	0001-000038	0207-000011	0433-000200	0933-000136
0002-000104	0045-000103	0088-000133	0342-000069	0398-000133	0003-000116	0208-000004	0434-000023	0941-000201
0002-000148	0045-000109	0090-000006	0343-000126	0398-000150	0005-000033	0208-000016	0434-000182	0941-000488
0003-000077	0048-000014	0090-000029	0345-000090	0398-000171	0005-000071	0214-000025	0439-000010	0966-000017
0003-000090	0048-000029	0090-000129	0345-000106	0398-000178	0005-000083	0222-000098	0439-000041	0966-000042
0004-000081	0048-000239	0091-000006	0345-000118	0398-000182	0005-000095	0230-000082	0439-000063	0966-000052
0005-000030	0051-000017	0091-000070	0345-000251	0398-000195	0006-000042	0234-000065	0439-000067	0966-000068
0005-000057	0051-000043	0092-000034	0345-000257	0398-000209	0006-000108	0241-000105	0439-000095	0966-000073
0006-000015	0051-000083	0093-000074	0346-000014	0398-000216	0008-000042	0250-000032	0449-000007	0966-000107
0006-000109	0051-000093	0093-000120	0346-000038	0398-000218	0012-000018	0294-000127	0449-000009	0966-000137
0008-000061	0051-000108	0094-000357	0346-000090	0398-000219	0012-000040	0315-000057	0485-000028	0966-000154
0009-000090	0051-000111	0095-000062	0347-000033	0399-000021	0012-000067	0337-000012	0485-000100	0981-000214
0009-000162	0052-000017	0096-000004	0347-000049	0400-000095	0012-000073	0345-000029	0485-000171	0981-000236
0009-000177	0052-000032	0096-000050	0347-000117	0403-000303	0012-000081	0345-000101	0485-000208	0981-000297
0010-000266	0052-000159	0097-000003	0349-000051	0405-000161	0013-000101	0346-000035	0498-000381	0981-000370
0011-000041	0053-000060	0099-000001	0349-000110	0406-000170	0014-000038	0346-000041	0515-000003	0981-000422
0011-000077	0054-000020	0099-000003	0352-000140	0406-000255	0014-000070	0346-000068	0538-000126	0999-000045
0011-000096	0054-000080	0099-000024	0352-000236	0406-000368	0016-000004	0347-000090	0560-000039	0999-000048
0012-000047	0054-000122	0099-000058	0353-000026	0406-000445	0016-000042	0347-000094	0576-000069	0999-000129
0012-000051	0055-000012	0099-000068	0353-000076	0406-000458	0016-000044	0347-000116	0590-000047	0999-000145
0012-000059	0055-000020	0107-000062	0356-000101	0409-000256	0016-000063	0348-000008	0590-000118	0999-000157
0012-000065	0055-000026	0108-000109	0356-000117	0411-000004	0016-000130	0348-000019	0602-000109	0999-000212
0012-000070	0055-000032	0109-000104	0356-000160	0411-000031	0027-000095	0348-000038	0618-000238	0999-000224
0012-000076	0055-000060	0111-000111	0356-000181	0411-000043	0031-000031	0348-000062	0618-000249	1010-000110
0012-000100	0055-000128	0124-000025	0358-000143	0411-000060	0031-000119	0348-000077	0630-000007	1010-000144
0012-000101	0056-000054	0124-000061	0358-000264	0411-000079	0033-000065	0351-000051	0642-000011	1010-000145
0012-000106	0056-000080	0124-000082	0360-000030	0411-000097	0035-000110	0352-000033	0665-000034	1010-000206
0013-000038	0056-000130	0126-000026	0360-000076	0411-000330	0035-000119	0352-000240	0673-000006	1010-000254
0013-000065	0056-000157	0126-000059	0360-000083	0412-000214	0042-000001	0352-000260	0673-000044	
0015-000197	0056-000227	0128-000038	0360-000192	0412-000216	0042-000118	0355-000022	0673-000073	
0016-000066	0059-000031	0128-000063	0365-000083	0416-000033	0044-000015	0356-000011	0673-000248	
0016-000067	0059-000075	0128-000085	0375-000092	0416-000050	0044-000027	0356-000016	0673-000279	
0016-000082	0059-000097	0129-000039	0375-000338	0416-000132	0045-000080	0356-000083	0673-000410	
0016-000098	0060-000016	0129-000058	0375-000378	0419-000084	0045-000086	0360-000091	0688-000002	
0017-000203	0060-000104	0132-000002	0379-000051	0420-000185	0046-000053	0360-000113	0705-000264	
0018-000118	0061-000031	0132-000106	0380-000084	0423-000107	0046-000087	0360-000132	0705-000322	
0020-000123	0061-000090	0135-000006	0381-000078	0424-000030	0046-000104	0360-000156	0720-000172	
0020-000168	0063-000005	0135-000035	0385-000003	0424-000100	0048-000026	0360-000243	0720-000225	
0021-000070	0063-000067	0141-000020	0385-000062	0424-000242	0048-000139	0360-000258	0720-000256	
0024-000004	0063-000076	0141-000064	0385-000074	0426-000103	0048-000188	0360-000278	0732-000057	
0024-000080	0063-000108	0141-000152	0385-000080	0427-000128	0048-000189	0365-000002	0732-000062	
0026-000050	0065-000036	0142-000058	0385-000183	0427-000207	0055-000073	0365-000067	0732-000133	
0026-000087	0065-000042	0142-000157	0385-000236	0429-000037	0055-000086	0368-000016	0743-000132	
0026-000108	0067-000202	0143-000027	0385-000257	0429-000099	0056-000170	0368-000018	0743-000201	
0026-000136	0068-000005	0144-000114	0385-000271	0429-000247	0056-000192	0368-000027	0750-000005	
0026-000162	0068-000165	0145-000090	0385-000415	0429-000251	0061-000074	0368-000035	0750-000037	
0026-000186	0070-000058	0197-000085	0386-000361	0432-000074	0061-000075	0368-000059	0750-000107	
0027-000048	0070-000069	0197-000086	0386-000405	0434-000030	0063-000112	0368-000071	0759-000099	
0027-000079	0070-000073	0199-000091	0386-000455	0434-000222	0064-000122	0375-000033	0776-000273	
0027-000119	0070-000075	0206-000014	0387-000081	0434-000375	0068-000139	0375-000170	0788-000037	
0029-000241	0070-000099	0206-000044	0388-000017	0434-000377	0070-000095	0379-000039	0788-000039	
0030-000002	0072-000065	0206-000050	0388-000167	0434-000378	0075-000245	0380-000021	0788-000143	
0030-000036	0072-000094	0208-000018	0390-000041	0438-000022	0076-000037	0380-000037	0798-000025	
0030-000071	0073-000064	0208-000074	0390-000079	0438-000050	0076-000047	0380-000131	0798-000059	
0030-000088	0074-000043	0209-000065	0392-000101	0438-000495	0076-000109	0380-000165	0798-000068	
0031-000011	0075-000048	0209-000125	0392-000202	0439-000087	0081-000036	0381-000003	0806-000004	
0031-000042	0075-000081	0210-000061	0392-000224	0439-000094	0093-000035	0386-000113	0806-000022	
0031-000085	0075-000095	0214-000032	0394-000072	0443-000093	0099-000089	0386-000354	0806-000071	
0031-000106	0076-000133	0214-000033	0394-000141	0443-000151	0099-000103	0386-000371	0806-000178	
0033-000096	0076-000151	0214-000051	0394-000209	0443-000385	0105-000005	0390-000038	0820-000044	
0034-000137	0076-000249	0215-000044	0394-000213	0443-000505	0105-000077	0395-000079	0838-000027	
0035-000011	0076-000282	0215-000180	0395-000113	0445-000061	0107-000022	0395-000085	0838-000123	
0035-000085	0076-000294	0220-000031	0398-000018	0448-000015	0111-000025	0398-000100	0838-000213	
0036-000153	0080-000079	0222-000079	0398-000040	0448-000287	0112-000009	0398-000186	0838-000292	
0036-000230	0081-000080	0225-000044	0398-000041	0449-000089	0113-000128	0400-000025	0838-000299	
0038-000001	0083-000184	0225-000048	0398-000050	0450-000077	0122-000024	0400-000040	0854-000293	
0038-000017	0085-000017	0227-000062	0398-000057	0451-000051	0126-000107	0400-000046	0866-000007	
0040-000014	0085-000041	0229-000105	0398-000079	0451-000056	0128-000184	0400-000049	0883-000326	
0040-000100	0085-000068	0232-000005	0398-000081	0451-000117	0129-000060	0400-000075	0898-000049	
0042-000043	0085-000089	0232-000076	0398-000091	0452-000081	0129-000117	0400-000083	0901-000096	
0042-000075	0085-000100	0235-000071	0398-000092	0452-000218	0135-000102	0411-000219	0912-000043	
0042-000091	0086-000099	0310-000036	0398-000099	0452-000297	0137-000059	0411-000287	0912-000119	
0042-000114	0086-000215	0317-000099	0398-000106		0139-000069	0420-000012	0912-000153	
0043-000002	0087-000050	0329-000080	0398-000113		0144-000038	0423-000167	0912-000168	
0044-000096	0087-000066	0329-000097	0398-000115		0144-000073	0427-000233	0912-000228	
0045-000019	0088-000073	0335-000053	0398-000125		0197-000078	0433-000178	0933-000108	

Received: 4 February 2020 Accepted: 8 June 2020
Published online: 17 June 2020

References

1. Siegel RL, Miller KD, Jemal A. Cancer statistics, 2019. CA Cancer J Clin. 2019;69(1):7–34.
2. Fan L, et al. Multidetector CT features of pulmonary focal ground-glass opacity: differences between benign and malignant. Br J Radiol. 2012;85(1015):897–904.
3. Henschke CI, et al. Survival of patients with stage I lung cancer detected on CT screening. N Engl J Med. 2006;355(17):1763–71.

4. Kuhnigk J-M, et al. Morphological segmentation and partial volume analysis for volumetry of solid pulmonary lesions in thoracic CT scans. IEEE Trans Med Imaging. 2006;25(4):417–34.
5. Aoyama M, et al. Computerized scheme for determination of the likelihood measure of malignancy for pulmonary nodules on low-dose CT images. Med Phys. 2003;30(3):387–94.
6. Kubota T, et al. Segmentation of pulmonary nodules of various densities with morphological approaches and convexity models. Med Image Anal. 2011;15(1):133–54.
7. Dehmeshki J, et al. Segmentation of pulmonary nodules in thoracic CT scans: a region growing approach. IEEE Trans Med Imaging. 2008;27(4):467–80.
8. Nithila EE, Kumar SS. Segmentation of lung nodule in CT data using active contour model and Fuzzy C-mean clustering. Alexandria Eng J. 2016;55(3):2583–8.
9. Ciompi F, et al. Towards automatic pulmonary nodule management in lung cancer screening with deep learning. Sci Rep. 2017;7:46479.
10. Yang Y, et al. Deep learning aided decision support for pulmonary nodules diagnosing: a review. J Thorac Dis. 2018;10(Suppl 7):S867.
11. Kostis WJ, et al. Three-dimensional segmentation and growth-rate estimation of small pulmonary nodules in helical CT images. IEEE Trans Med Imaging. 2003;22(10):1259–74.
12. Diciotti S, et al. Automated segmentation refinement of small lung nodules in CT scans by local shape analysis. IEEE Trans Biomed Eng. 2011;58(12):3418–28.
13. Farag AA, et al. A novel approach for lung nodules segmentation in chest CT using level sets. IEEE Trans Image Process. 2013;22(12):5202–13.
14. Keshani M, et al. Lung nodule segmentation and recognition using SVM classifier and active contour modeling: A complete intelligent system. Comput Biol Med. 2013;43(4):287–300.
15. Li B, et al. Segmentation of pulmonary nodules using adaptive local region energy with probability density function-based similarity distance and multi-features clustering. Biomed Eng Online. 2016;15(1):49.
16. Ye W, Gu W, Guo X, et al. Detection of pulmonary ground-glass opacity based on deep learning computer artificial intelligence. Biomed Eng Online. 2019;18(1):6.
17. Roy R, Chakraborti T, Chowdhury A. A deep learning-shape driven level set synergism for pulmonary nodule segmentation. Pattern Recogn Lett. 2019;123:31–8.
18. Wang S, et al. Central focused convolutional neural networks: developing a data-driven model for lung nodule segmentation. Med Image Anal. 2017;40:172–83.
19. Xu J, Monaco JP, Madabhushi A. Markov random field driven region-based active contour model (MaRACel): application to medical image segmentation. In: International conference on medical image computing and computer-assisted intervention. Berlin, Heidelberg: Springer; 2010.
20. Xu J, et al. Connecting Markov random fields and active contour models: application to gland segmentation and classification. J Med Imaging. 2017;4(2):021107.
21. Shahvaran Z, et al. Variational level set combined with Markov random field modeling for simultaneous intensity non-uniformity correction and segmentation of MR images. J Neurosci Methods. 2012;209(2):280–9.
22. Zhu Y, et al. Automatic segmentation of ground-glass opacities in lung CT images by using Markov random field-based algorithms. J Digit Imaging. 2012;25(3):409–22.
23. Armato III, Samuel G, et al. The lung image database consortium (LIDC) and image database resource initiative (IDRI): a completed reference database of lung nodules on CT scans. Med Phys. 2011;38(2):915–31.
24. Li Wang, et al. Active contours driven by local Gaussian distribution fitting energy. Signal Process. 2009;89(12):2435–47.
25. Li BN, et al. Integrating spatial fuzzy clustering with level set methods for automated medical image segmentation. Comput Biol Med. 2011;41(1):1–10.
26. Lankton Shawn, Tannenbaum Allen. Localizing region-based active contours. IEEE Trans Image Process. 2008;17(11):2029–39.
27. Achuthan A, et al. Wavelet energy-guided level set-based active contour: A segmentation method to segment highly similar regions. Comput Biol Med. 2010;40(7):608–20.
28. Yang Z, Zhu Z, Ma J. Image classification algorithm based on iterative optimization of conjugate gradient method. J Guilin Univ Electron Technol. 2019;39(06):494–7.
29. Geng Z, Zhu Z, Huang Q. An improved SQP algorithm for mathematical programs with nonlinear complementarity constraints. J Guilin Univ Electron Technol. 2011;31(06):494–7.
30. Yang X, et al. An efficient MRF embedded level set method for image segmentation. IEEE Trans Image Process. 2014;24(1):9–21.
31. Ji Z, et al. Active contours driven by local likelihood image fitting energy for image segmentation. Inf Sci. 2015;301:285–304.
32. Liu B, et al. Probability density difference-based active contour for ultrasound image segmentation. Pattern Recogn. 2010;43(6):2028–42.
33. Kokkinos Iasonas, Maragos Petros. Synergy between object recognition and image segmentation using the expectation-maximization algorithm. IEEE Trans Pattern Anal Mach Intell. 2009;31(8):1486–501.
34. Xiao D, et al. A region and gradient based active contour model and its application in boundary tracking on anal canal ultrasound images. Pattern Recogn. 2007;40(12):3522–39.
35. Li C et al. Level set evolution without re-initialization: a new variational formulation. In: 2005 IEEE computer society conference on computer vision and pattern recognition (CVPR'05). Vol. 1. New York: IEEE; 2005.

Publisher's Note